



Effect of material stiffness on hardness: a computational study based on model potentials

Gerolf Ziegenhain, H.M. Urbassek

► To cite this version:

Gerolf Ziegenhain, H.M. Urbassek. Effect of material stiffness on hardness: a computational study based on model potentials. Philosophical Magazine, 2009, 89 (26), pp.2225-2238. 10.1080/14786430903022697 . hal-00514028

HAL Id: hal-00514028

<https://hal.science/hal-00514028>

Submitted on 1 Sep 2010

HAL is a multi-disciplinary open access archive for the deposit and dissemination of scientific research documents, whether they are published or not. The documents may come from teaching and research institutions in France or abroad, or from public or private research centers.

L'archive ouverte pluridisciplinaire **HAL**, est destinée au dépôt et à la diffusion de documents scientifiques de niveau recherche, publiés ou non, émanant des établissements d'enseignement et de recherche français ou étrangers, des laboratoires publics ou privés.



Effect of material stiffness on hardness: a computational study based on model potentials

Journal:	<i>Philosophical Magazine & Philosophical Magazine Letters</i>
Manuscript ID:	TPHM-09-Mar-0119.R1
Journal Selection:	Philosophical Magazine
Date Submitted by the Author:	05-May-2009
Complete List of Authors:	Ziegenhain, Gerolf; University Urbassek, H.M.; University, Physics
Keywords:	hardness, molecular dynamics, nanoindentation
Keywords (user supplied):	hardness, molecular dynamics, nanoindentation



Effect of material stiffness on hardness: a computational study
based on model potentials

Gerolf Ziegenhain and Herbert M. Urbassek*

*Fachbereich Physik und Forschungszentrum OPTIMAS, Universität Kaiserslautern,
Erwin-Schrödinger-Straße, D-67663 Kaiserslautern, Germany*

(Dated: May 6, 2009)

Abstract

We investigate the dependence of the hardness of materials on their elastic stiffness. This is possible by constructing a series of model potentials of the Morse type; starting on modelling natural Cu, the model potential exhibits an increased elastic modulus, while keeping all other potential parameters (lattice constant, bond energy) unchanged. Using molecular-dynamics simulation, we perform nanoindentation experiments on these model crystals. We find that the crystal hardness scales with the elastic stiffness. Also the load drop, which is experienced when plasticity sets in, increases in proportion to the elastic stiffness, while the yield point, i.e., the indentation at which plasticity sets in, is independent of the elastic stiffness.

PACS numbers: 62.20.-x, 81.40.Jj

Keywords: Molecular dynamics, hardness, nanoindentation

I. INTRODUCTION

While the elastic properties of solids are well understood, and their description in terms of interatomic potentials is well established, plastic deformation of solids – and the concurrent phenomena of dislocation generation and motion – are more complex and their modelling presents greater difficulties. One reason certainly is that plasticity involves strongly non-equilibrium states in the solid, in which the material is stressed so far that interatomic bonds are broken and new bonds are formed.

The simplest quantitative measure of plasticity is given by the material hardness, i.e., the pressure with which the material withstands plastic deformation. It has long been known that the hardness of a defect-free, ideal crystal, the theoretical strength, is proportional to the material's shear modulus. This important result, which dates back to Frenkel,^{1,2} has been derived by considering the shear stress necessary to induce slip in a perfect lattice; modern ab initio quantum-mechanical calculations have confirmed this result.^{3–5} However, the question remains how the elastic stiffness of a material influences dislocation generation and the emergence of plasticity in a more complex and realistic situation.

We choose a nanoindentation scenario to investigate the onset of plasticity, and its dependence on the material stiffness. A molecular-dynamics simulation allows to provide atomistic insight into the reaction of a material to an applied load, to calculate the force-depth curve and to extract the contact pressure and the material hardness. It furthermore allows to describe in detail the induced damaged patterns, such as the formation of stacking faults and dislocation loops.

Our study is based on the Morse interatomic potential. While it is well known that metals cannot be described in all details by pair potentials,⁶ this class of potentials readily allows to generate a series of potentials, which all describe the same material, in which, however, exactly one property is arbitrarily changed. Since the prime aim of our study is to inquire into the generic dependence of plasticity and hardness on the elastic stiffness of the material, rather than to describe one particular material as accurately as possible, our choice of a Morse potential appears appropriate. We note that the Morse potential has been used previously to describe dislocations in metals.^{7–9}

II. METHOD

A. Potentials

We use the Morse potential

$$V(r) = D \{ \exp [-2\alpha(r - r_0)] - 2 \exp [-\alpha(r - r_0)] \} \quad (1)$$

to model our material. It is characterized by three parameters: the bond strength D , the equilibrium bond distance of the dimer, r_0 , and the potential fall-off α . As is well known,^{6,10} the Morse potential cannot describe all characteristics of bonding in metals; however, as discussed elsewhere,¹¹ it can give a reasonable description of the elastic^{12,13} and also plastic processes occurring under indentation. We adopted this potential, since it allows to fit in a transparent way the materials properties. Since the Morse potential contains three parameters, it is possible to fit it to three materials properties; these are traditionally chosen as the lattice constant a , the cohesive energy E_{coh} , and the bulk modulus B .

For example, Cu with¹⁴ $a = 3.615 \text{ \AA}$, $E_{\text{coh}} = 3.54 \text{ eV}$, and $B = 134.4 \text{ GPa}$ can be described by a Morse potential with $D = 0.337 \text{ eV}$, $r_0 = 2.89 \text{ \AA}$, and $\alpha = 1.33 \text{ \AA}^{-1}$. We note that here and in the following, we cut off the potential at $r_{\text{cut}} = 2.5a = 9.0375 \text{ \AA}$ – i.e. including 248 neighbours – , and shift the potential to zero at this distance.

We create a series of Morse potentials, in which the lattice constant and cohesive energy are kept unchanged, but the bulk modulus is set to a preassigned value. These potentials can hence be considered as describing a series of *pseudo-Cu* materials with identical cohesion, but changed bulk moduli. Table 1 reproduces the values of the fit parameters obtained for the potentials employed in this study. We use a Levenberg-Marquardt based optimization for parameter fitting; the values of a (E_{coh}) are reproduced within 0.1 % (1%).

Of course, by changing these parameters all other physical properties of the crystals will also be changed; in the following, we discuss the (linear) elastic properties and the generalized stacking fault energy, since these are of prime interest for nanoindentation. We note that in particular the third-order elastic constants will change, and hence the nonlinear response to indentation; however, the Morse potential is known¹³ not to give realistic values for these constants, and hence we refrain from further discussion. Interestingly, when the bulk modulus is changed by a factor of 14.7, the dimer bond strength increases by a factor

of only 3, for fixed cohesive energy. This reflects an increased nearest-neighbor bonding, and is accordingly accompanied by a steeper potential fall-off.

The linear elastic properties of an fcc crystal are given by 3 elastic constants, c_{11} , c_{12} , and c_{44} . However, for a pair potential, it is always $c_{12} = c_{44}$, so that only two elastic constants describe the elastic behaviour. We chose the bulk modulus

$$B = \frac{c_{11} + 2c_{12}}{3} \quad (2)$$

and the average shear modulus

$$G = \frac{c_{11} + 2c_{44} - c_{12}}{5} \quad (3)$$

to describe the elastic properties. For real Cu, it is $G = 39.8$ GPa.¹⁴ Table 1 shows the shear moduli obtained for pseudo-Cu, and Fig. 1 demonstrates that G increases quite linearly with B ; only for the highest moduli, G increases superlinearly with B . So in general, we may say that the entire elastic behaviour (the elastic stiffness) of pseudo-Cu changes in correspondence with B ; we shall talk of *weak* and *strong* materials.

B. Generalized stacking fault energy

The generalized stacking fault (GSF) energy can be used to characterize the behaviour of a material with respect to the formation of stacking faults, and hence dislocation formation and glide.^{8,15–18} For its definition, we consider an fcc crystal, whose upper part has glided along a (111) plane with respect to its lower part by a definite amount; in the present paper we only consider glide vectors along the $[11\bar{2}]$ direction. The GSF energy is the potential energy per surface area of the deformed crystal; when determining this energy, relaxation of the crystal vertical to the (111) plane, but no relaxation or reconstruction within this plane is allowed for.^{8,16} In our calculation, it proved necessary to choose the crystallite rather large, 10 lattice constants in vertical direction and 25 lattice constants in both lateral directions; we employed the conjugate-gradient technique to relax the crystal in vertical direction.

Fig. 2 displays the variation of the GSF surface, γ , along the $[11\bar{2}]$ (111) displacement. The minimum at 0 displacement corresponds to fcc stacking; here $\gamma = 0$ by definition. The second minimum is found for a displacement corresponding to a partial Burgers vector $\frac{1}{6}[\bar{1}\bar{1}2]a = a/\sqrt{6} \cong 1.5$ Å. It describes a stacking fault with the stable stacking fault energy

γ_s . For our potentials, extremely small values were obtained, which varied in the range of $\gamma_s = (-2 \cdots +2)$ mJ/m². For comparison, the experimental value of γ_s for Cu is 45 mJ/m²;^{19,20} this value is retrieved by ab initio calculations.^{3,4} We note that in previous investigations,⁷ a sufficiently large value of the stacking fault energy could only be obtained by adapting the value of the cut-off radius to $r_{\text{cut}} = 2.2a$; for larger r_{cut} , γ_s strongly decreased.

We found that the exact determination of γ_s is nontrivial, since large crystallites have to be relaxed; sometimes only a local and not the global energy minimum may have been found. Furthermore, it is known that the stacking fault energy may depend sensitively on the cut-off radius of the potential.⁷ Hence we conclude that within the Morse pair potential approximation, the stable stacking fault energy of fcc metals (of Cu, at least) is strongly underestimated. It does not – or only negligibly – depend on the elastic stiffness of the material.

The energy barrier between the fcc crystal position and the stable stacking fault is called the unstable stacking fault energy, γ_u . It depends strongly on the elastic stiffness. As Fig. 3 shows, it increases roughly linearly with the bulk modulus B , and hence also with the shear modulus G , cf. Fig. 1. This may be understood since the displacement of two (111) planes in the crystal corresponds to a gliding motion; thus the barrier to gliding, γ_u , is strongly correlated with the shear modulus. The latter feature has been demonstrated explicitly using ab initio data in Fig. 11 of Ref. 18. We demonstrate in the Appendix that γ_u is directly connected to the nucleation of stacking faults.

C. Indentation

In order to model the plastic deformation of our material, we performed indentation simulations using an appropriately adapted version of the LAMMPS molecular-dynamics code.²¹ Our target consists of an fcc crystallite with a (100) surface; it has a depth of 25 nm and a square surface area of 621.2 nm²; it contains 1325598 atoms. Lateral periodic boundary conditions have been applied. At the bottom, atoms in a layer of the width r_{cut} have been constrained to $F_{\text{normal}} = 0$. Since all potentials used in the present investigation predict the same equilibrium lattice constant, these boundary conditions can be applied identically for all our potentials. Before starting the simulations, the substrates are relaxed to minimum energy.

The indenter is modelled as a soft sphere of radius R . We chose a non-atomistic representation of the indenter, since we are not interested in the present study in any atomistic displacement processes occurring in the indenter, but only in the substrate. The interaction potential between the indenter and the substrate atoms is modelled by a repulsive potential²²

$$V(r) = \begin{cases} k(R - r)^3, & r < R, \\ 0, & r \geq R, \end{cases} \quad (4)$$

since we are in this generic study not interested in the complexities introduced by adhesion phenomena. The indenter stiffness was set to $k = 3 \text{ eV}/\text{\AA}^3$. This value was determined in a series of simulations as a compromise such that (i) it is hard enough in comparison to the substrate stiffness (note that a finite indenter stiffness enters into the force-displacement curve, Eq. (5), via a modified reduced modulus), and (ii) it is soft enough to allow stable solutions of the molecular-dynamics equations. Our indenter has a radius of $R = 8 \text{ nm}$. Indentation proceeds in the so-called *velocity-controlled* approach,²² in which the indenter proceeds with a fixed velocity, $v = 20 \text{ m/s}$ in our case, into the substrate. As a consequence of the energy input by the indenter, the substrate temperature increases from initially 0 K to a maximum value of 10 K in the course of the simulation.

III. RESULTS

A. Force-displacement curves

Fig. 4 shows the basic result of the simulation, the force-displacement curves. In all these curves it is seen that the force F increases monotonically with the displacement d into the substrate until a depth d_{yield} which is about $9.4 \pm 0.5 \text{ \AA}$ and where the force suddenly drops. This corresponds to the onset of plastic deformation inside the material. The first, monotonically increasing part of the curve is due to elastic deformation of the substrate. Hertz²³ calculated that for an elastically isotropic solid it holds

$$F = \frac{4}{3} E_r d^{3/2} \sqrt{R}. \quad (5)$$

In this relation, a single materials parameter, the so-called reduced modulus E_r , describes the materials elastic response.^{24,25} For a rigid indenter, it may be expressed in terms of the

Young's modulus E and the Poisson ratio ν of the substrate as

$$E_r = \frac{E}{1 - \nu^2}. \quad (6)$$

We test this law in Fig. 4b. To do so, we need to calculate the reduced elastic modulus for a (100) surface. Here, Young's modulus and the Poisson ratio have to be calculated for deformation in (100) direction, perpendicular to the surface. The corresponding formulae are rather complex and are provided in Ref. 26. Fig. 4b shows that in the range of $G = 80 - 180$ GPa, the elastic behaviour follows well the (generalized) Hertz law (5). Only for the extreme cases of $G = 39$ and 278 GPa, the normalized forces F/E_r are too small. We believe that this deviation from the Hertz law is due to (i) a poorer quality of the potential to describe the materials reaction, and (ii) in particular in the case of the weaker pseudo-Cu, $G = 39$ GPa, due to the softness of the substrate, which makes the fluctuations in the response of the substrate to the constant-velocity indentation more sizable. We note that when normalizing F/G , an equally satisfactory uniformity of the curves is achieved; we do not show this plot, since the theoretical foundation appears to be missing.

It may appear astonishing that Hertz' continuum result (5) and atomistic simulation are in such close agreement with each other. We note that a recent study²⁷ investigated the appropriateness of continuum modelling for contact problems and found close agreement with atomistic simulation – even on the scale of a few lattice constants.

At the yield point the force drops suddenly due to the onset of plasticity; this well-known phenomenon is called the *load drop*. In our series of simulations we saw that the exact position of the yield point d_{yield} does not show a monotonic trend with the elastic stiffness of the substrate; rather d_{yield} fluctuates. We believe that in this constant-velocity indentation, the yield point may be subject to fluctuations in the simulation procedure. We therefore conclude that within the limits of the fluctuations the position of the yield point does not depend on the elastic stiffness of the target.

However, the load drop shows a clear increase with the elastic stiffness of the material. This is understandable since the atomistic reason for the load drop is the nucleation of a stacking fault in the material and the propagation of the emerging dislocation away from the highly stressed region immediately below the indenter. Stacking-fault generation requires an energy which scales with the unstable stacking fault energy, γ_u , which has been found to scale well with the elastic stiffness. Fig. 4b then points out that stress relief ('load drop') is

proportional to the elastic stiffness.

B. Hardness

The normal force F divided by the (projected) contact area A of the indenter, projected onto the original surface plane, defines the contact pressure p . We calculate A from the ensemble of contact atoms of the indenter, which are farthest away from the indentation axis, and approximating it as an ellipse. After the onset of plasticity, it gives the hardness of the material. Hertz also determined the contact pressure p to be proportional to the substrate elastic modulus,

$$p = \frac{4}{3\pi} E_r \sqrt{\frac{d}{R}}. \quad (7)$$

Fig. 5 shows the simulation results for the contact pressure. In view of the predicted proportionality (7) and the good quality of the scaling with the material stiffness, which we observed in Fig. 4, we present our data scaled with the shear modulus G . This is also motivated by the consideration that the theoretical shear strength τ of the material is given by

$$\tau = \epsilon G, \quad (8)$$

where ϵ is a constant, which depends on the crystal structure of the solid but is otherwise quite material-independent. Frenkel estimated $\epsilon = 1/(2\sqrt{2}\pi) = 0.11$ for the important $\langle 112 \rangle$ $\{111\}$ glide system of fcc metals.² Recent more refined estimates based on density functional theory give a slightly reduced value, $\epsilon = 0.085$.³⁻⁵

Tabor showed that the hardness measured as the contact pressure during nanoindentation amounts to 3τ ,^{2,28} since the nanoindentation acts as a ‘lens’ focussing the stress in a small volume beneath the contact point.²⁹ Using Eq. (8), we hence expect

$$H = 3\tau = 3\epsilon G. \quad (9)$$

Fig. 5 shows that after the onset of plasticity, the hardness is indeed proportional to the shear modulus and well described by Eq. (9) with a coefficient of $0.2 - 0.25$, i.e., $\epsilon = 0.07 - 0.08$, in satisfactory agreement with the estimates of ϵ given above.. The figure also

appears to indicate that the pressure fluctuations in the fully plastically regime are smaller for soft materials, which appears plausible.

Note that also in the elastic regime, the scaled contact pressure p/G lies on one single curve, again underlining the importance of the shear modulus for the indentation behaviour. The only exception is given by the softest material. In this case the energy difference between the fcc and the hcp structures is rather small, and we observe instabilities at the relaxed free surface of the crystallite, which are reflected in the hardness curve, Fig. 5.

C. Plasticity

Figs. 6 and 7 give an atomistic presentation of the dislocations which developed in the substrate after the onset of plasticity. We analyzed the local atomic structures using a method based on the angular correlation of nearest-neighbour atoms.³⁰ We found this method to be superior for our purposes to the more common analysis based on the centrosymmetry parameter.²² Only atoms deviating from the fcc structure are visualized: atoms in stacking faults (red) are surrounded by unidentifiable structures of atoms in low-symmetry structures (grey) and a very small amount of atoms in bcc coordination (green). These grey and green atoms mark the boundaries of the dislocation loops due to the strong lattice deformations existing there. The free surface is also coloured grey.

A few general remarks on dislocation nucleation and activity, which were observed for all the potentials investigated here, are in order: In all cases, dislocations nucleate below the surface, i.e., homogeneously in the material. After nucleation, we first observe the emission of leading Shockley partials, in other words, the $\langle \bar{1}\bar{1}2 \rangle \{111\}$ glide system was activated first. After the ensuing nucleation of the trailing Shockley partials, the full dislocation loops activate the $\langle 1\bar{1}0 \rangle \{111\}$ glide system. These findings are in agreement with many earlier atomistic simulations of nanoindentation of metals.^{22,31,32} As discussed in detail in Ref. 33, the early emission of partial dislocations is typical of a material with a small ratio of γ_s/γ_u , since the creation of the trailing partial costs considerable energy compared to the surface energy of the created stacking fault. Only for ratios $\gamma_s/\gamma_u \cong 1$, the immediate creation of full dislocations would be favoured.

Fig. 6 displays the plasticity shortly after the nucleation of the first dislocations. The two materials shown here have a similar yield point (cf. Fig. 4), so that the amount of dislocated

material can be compared. For the stiffer material, the damage is more concentrated around the indenting sphere. On the other hand, for the softer material the size of the dislocation loops has increased. For fully developed plasticity (Fig. 7) we observe how prismatic dislocation loops have formed and were driven away from the indenter. We emphasize that the changed elastic stiffness in our model crystals does not influence the type of dislocations nucleated nor which glide systems are activated.

Finally, we mention that for fully developed plasticity (Fig. 7) the elastic stiffness does affect the form and size of the plastic zones. For smaller elastic stiffness, (Fig. 7a), evidently *more* and *smaller* loops have been generated. This is in agreement with our finding that for smaller stiffness, also the unstable stacking fault energy – and hence the barrier to dislocation formation and slip – is smaller: hence we have *more* loops. In contrast, for the stiffer material (Fig. 7b), the nucleation of loops is retarded, and fewer but *larger* loops are formed.

IV. SUMMARY

We set up a series of Morse potentials, which describe *pseudo-Cu* materials. In these, the lattice constant and cohesive energy coincides with that of Cu, while the bulk modulus B is systematically changed. We find that all elastic constants, and in particular the shear modulus, are changed roughly in proportion to the bulk modulus. Not surprisingly, the elastic part of the indentation curve scales with the elastic stiffness, as predicted by the Hertzian contact theory.

Also the contact pressure in the elastic regime, up to the yield point, is in good approximation proportional to the material stiffness; this is in agreement with Hertz' contact theory. As a consequence, the onset of plasticity and the mechanism of yield are found to be quite independent of the elastic stiffness. In our series of materials, the material yields after an indentation of roughly 9.2 Å with only little variation. Again this is understandable from simple Hertz contact theory, since the contact pressure is proportional to the substrate elastic stiffness. However, the load drop, that is the stress release due to the formation of plasticity increases in proportion to the elastic stiffness.

The hardness of the material, i.e., the pressure with which the material withstands plastic deformation. is found to be proportional to the elastic stiffness; this is agreement with the

established ideas of Frenkel and Tabor.^{1,2,28}

We find that for our series of potentials, also the unstable stacking fault energy γ_u , which parameterizes the energy barrier to form a stacking fault and hence plasticity, changes in proportion to the elastic stiffness. Accordingly, we observe that the plastic zones formed by indentation depend on this parameter: many small loops are formed in soft materials (small B and γ_u , while few but larger loops are formed in hard materials.

Acknowledgments

The authors acknowledge financial support by the Deutsche Forschungsgemeinschaft via the Graduiertenkolleg 814.

APPENDIX A: RELATION BETWEEN γ_u AND THE NUCLEATION OF STACKING FAULTS

The unstable stacking fault energy, γ_u , is defined as the maximum in the generalized stacking fault energy curve. We demonstrate in this Appendix by way of an example that γ_u is decisive for controlling the energetics of stacking fault nucleation in nanoindentation.

To this end we determine in a representative nanoindentation simulation the time $t_{sf} = 66.5$ ps when the first stacking fault forms. This stacking fault consists of $N = 159$ atoms and spans an area of $A_{sf} = 910.4 \text{ \AA}^2$. The energy barrier for forming the stacking fault then amounts to $E_{sf} = \gamma_u A_{sf}/N = 0.198 \text{ eV/atom}$ for the potential employed.²⁰ For our specific simulation, Fig. 8, E_{sf} and t_{sf} have been indicated.

We analyze the simulation and study in detail the time history of these N atoms which are eventually to form the stacking fault. Fig. 8 displays the time evolution of the potential energy per atom in this ensemble of N atoms; kinetic energies are of the order of 1 meV/atom in our system and hence negligible. Due to the strong fluctuations occurring, we display the average energy $\langle E \rangle$, fluctuations $\sigma(E)$ and the maximum. The important message of this figure is that the stacking fault nucleates at exactly that time where the average potential energy $\langle E \rangle$ stored in the substrate reaches the nucleation barrier E_{sf} . We note that at the time $t = 52.9$ ps, when the fluctuations $\sigma(E)$ reach the energy barrier E_{sf} , an amorphized zone (visible via the centrosymmetry parameter as a region in which the fcc lattice structure has been lost) appears, which is a precursor to stacking fault formation.

Certainly, this analysis cannot be used to *predict* when a stacking fault will be generated in a simulation, since the size of the forming stacking fault must be known before the analysis can be carried out; other studies investigated this issue.^{34,35} However, the analysis shows that the unstable stacking fault energy, γ_u , is the decisive parameter for describing the onset of plasticity in nanoindentation. For this reason, we took care to determine this parameter for the potentials used in the present study, cf. Fig. 3.

-
- * Electronic address: urbassek@rhrk.uni-kl.de; URL: <http://www.physik.uni-kl.de/urbassek/>
- ¹ J. Frenkel, Z. Phys. **37**, 572 (1926).
 - ² A. Kelly and N. H. Macmillan, *Strong Solids* (Clarendon Press, Oxford, 1986), 3rd ed.
 - ³ D. Roundy, C. R. Krenn, M. L. Cohen, and J. W. Morris, Phys. Rev. Lett. **82**, 2713 (1999).
 - ⁴ S. Ogata, J. Li, and S. Yip, Science **298**, 807 (2002).
 - ⁵ S. Ogata, J. Li, N. Hirotsaki, Y. Shibutani, and S. Yip, Phys. Rev. B **70**, 104104 (2004).
 - ⁶ A. E. Carlsson, in *Solid State Physics*, edited by H. Ehrenreich and D. Turnbull (Academic Press, Boston, 1990), vol. 43, p. 1.
 - ⁷ R. M. J. Cotterill and M. Doyama, Phys. Rev. **145**, 465 (1966).
 - ⁸ V. Vitek, Philos. Mag. **73**, 773 (1968).
 - ⁹ V. Vitek, Philos. Mag. A **58**, 193 (1988).
 - ¹⁰ M. Finnis, *Interatomic forces in condensed matter* (Oxford University Press, Oxford, 2003).
 - ¹¹ G. Ziegenhain, A. Hartmaier, and H. M. Urbassek, in preparation (2008).
 - ¹² L. A. Girifalco and V. G. Weizer, Phys. Rev. **114**, 687 (1959).
 - ¹³ R. C. Lincoln, K. M. Koliwad, and P. B. Ghate, Phys. Rev. **157**, 463 (1967).
 - ¹⁴ C. J. Smithells, *Metals reference handbook* (Butterworths, London, 1949).
 - ¹⁵ J. R. Rice, J. Mech. Phys. Sol. **40**, 239 (1992).
 - ¹⁶ D. Farkas, S. J. Zhou, C. Vaihne, B. Mutasa, and J. Panova, J. Mater. Res. **12**, 93 (1997).
 - ¹⁷ G. Lu, N. Kiuissis, V. V. Bulatov, and E. Kaxiras, Phys. Rev. B **62**, 3099 (2000).
 - ¹⁸ C. Brandl, P. M. Derlet, and H. Van Swygenhoven, Phys. Rev. B **76**, 054124 (2007).
 - ¹⁹ J. P. Hirth and J. Lothe, *Theory of dislocations* (Wiley, New York, 1982), 2nd ed.
 - ²⁰ Y. Mishin, M. J. Mehl, D. A. Papaconstantopoulos, A. F. Voter, and J. D. Kress, Phys. Rev. B **63**, 224106 (2001).
 - ²¹ <http://lammmps.sandia.gov/>.
 - ²² C. L. Kelchner, S. J. Plimpton, and J. C. Hamilton, Phys. Rev. B **58**, 11085 (1998).
 - ²³ H. Hertz, J. Reine Angew. Math. **92**, 156 (1882).
 - ²⁴ A. C. Fischer-Cripps, *Nanoindentation* (Springer, New York, 2004), 2nd ed.
 - ²⁵ A. C. Fischer-Cripps, *Introduction to Contact Mechanics* (Springer, New York, 2007), 2nd ed.

- 1
2
3
4
5
6
7
8
9
10
11
12
13
14
15
16
17
18
19
20
21
22
23
24
25
26
27
28
29
30
31
32
33
34
35
36
37
38
39
40
41
42
43
44
45
46
47
48
49
50
51
52
53
54
55
56
57
58
59
60
- ²⁶ J. Turley and G. Sines, J. Phys. D **4**, 264 (1971).
²⁷ B. Luan and M. O. Robbins, Nature **435**, 929 (2005).
²⁸ D. Tabor, *The hardness of metals* (Clarendon Press, Oxford, 1951).
²⁹ J. Li, MRS Bull. **32**, 151 (2007).
³⁰ G. J. Ackland and A. P. Jones, Phys. Rev. B **73**, 054104 (2006).
³¹ E. T. Lilleodden, J. A. Zimmermann, S. M. Foiles, and W. D. Nix, J. Mech. Phys. Sol. **51**, 901 (2003).
³² M. A. Tschopp, D. E. Spearot, and D. L. McDowell, Modelling Simul. Mater. Sci. Eng. **15**, 693 (2007).
³³ H. Van Swygenhoven, P. M. Derlet, and A. G. Frøseth, Nature Materials **3**, 399 (2004).
³⁴ J. Li, K. J. Van Vliet, T. Zhu, S. Yip, and S. Suresh, Nature **418**, 307 (2002).
³⁵ J. K. Mason, A. C. Lund, and C. A. Schuh, Phys. Rev. B **73**, 054102 (2006).

D (eV)	α (\AA^{-1})	r_0 (\AA)	B (GPa)	G (GPa)	γ_u (mJ/m ²)
0.203	0.90	3.47	67.7	39.2	71.8
0.272	1.12	3.10	98.6	58.6	89.9
0.320	1.28	2.93	124.2	74.4	85.8
0.337	1.33	2.89	134.4	80.5	113.8
0.359	1.41	2.83	145.9	88.2	96.2
0.390	1.54	2.77	178.7	106.5	118.9
0.416	1.65	2.72	197.7	118.9	135.9
0.437	1.76	2.69	227.3	136.0	163.5
0.455	1.86	2.66	244.5	147.4	181.6
0.471	1.96	2.64	269.0	162.3	203.3
0.484	2.05	2.63	300.7	180.4	228.9
0.495	2.13	2.62	325.2	194.9	248.6
0.504	2.22	2.61	351.1	210.5	268.8
0.513	2.30	2.60	369.8	222.6	283.1
0.520	2.38	2.60	412.4	246.2	315.3
0.526	2.45	2.59	420.5	252.7	320.2
0.532	2.52	2.59	458.3	274.1	348.0
0.537	2.59	2.58	460.9	277.8	348.6
0.555	2.92	2.57	590.0	354.8	433.8
0.563	3.16	2.57	720.0	430.4	516.3
0.571	3.38	2.56	772.7	465.7	538.1
0.589	3.54	2.56	881.5	530.3	599.9
0.591	3.73	2.56	990.1	594.5	655.3

TABLE I: Fitted parameters of the potentials, D , α , r_0 , cf. Eq. (1). Materials properties determined from these potentials, B , G , γ_u .

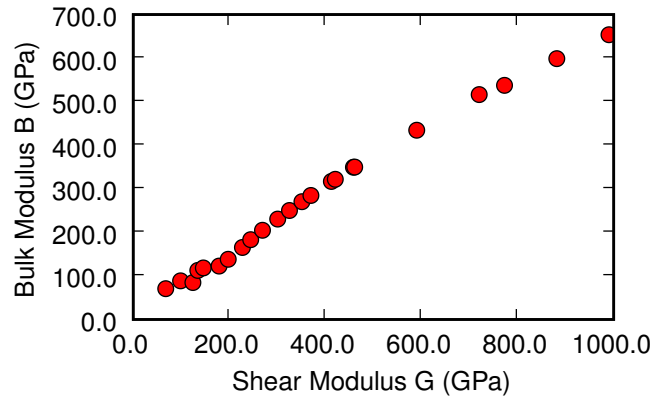


FIG. 1: Correlation between the shear modulus G and the bulk modulus B in the series of Morse potentials investigated.

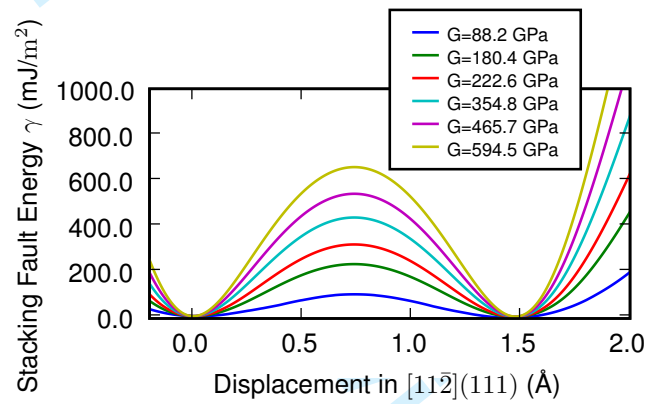


FIG. 2: Generalized stacking fault energy as a function of displacement in $[11\bar{2}]$ direction in the series of Morse potentials investigated.

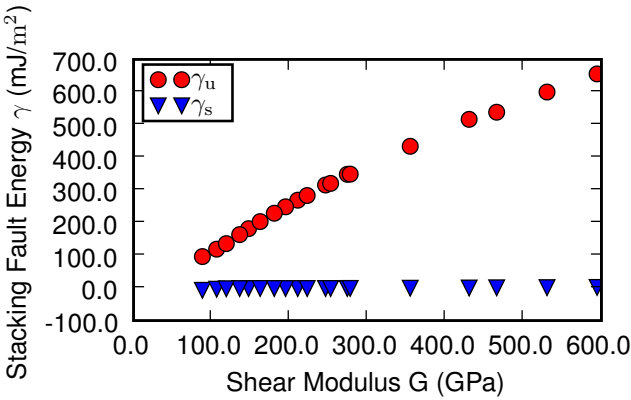
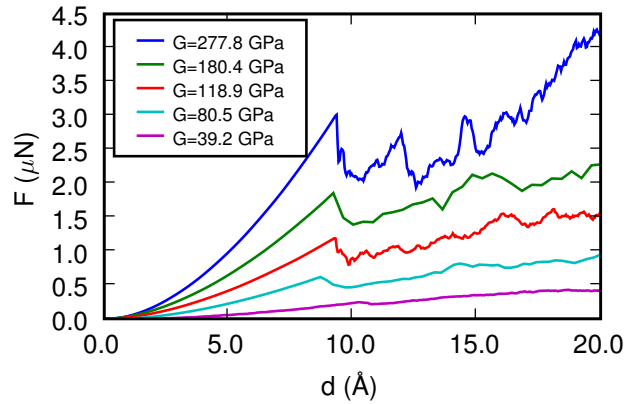
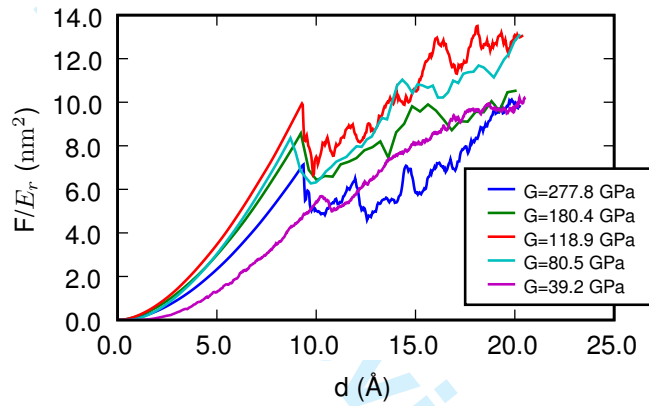


FIG. 3: Dependence of the stable and unstable stacking fault energies, γ_u and γ_s on the shear modulus G in the series of Morse potentials investigated.



(a)



(b)

FIG. 4: a) Dependence of the indentation force F on the indentation depth d in the series of Morse potentials investigated. b) Forces F normalized to the reduced elastic modulus E_r .

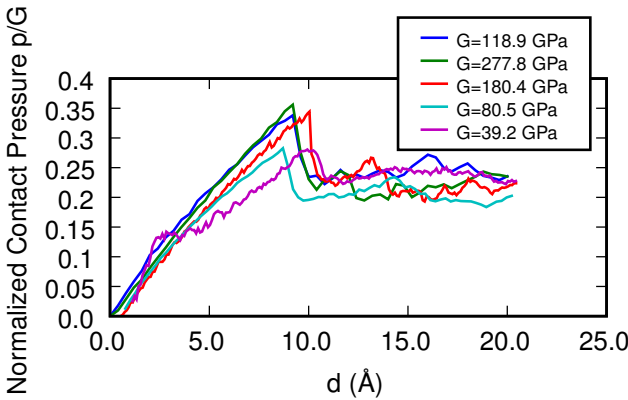


FIG. 5: Contact pressure p , normalized to the shear modulus G , as a function of indentation depth d in the series of Morse potentials investigated. After the onset of plasticity, the contact pressure defines the hardness of the material.